ADVANCED ENERGY MATERIALS

Supporting Information

for *Adv. Energy Mater.*, DOI: 10.1002/aenm.201703237

Bottom-Up Confined Synthesis of Nanorod-in-Nanotube Structured Sb@N-C for Durable Lithium and Sodium Storage

Wen Luo, Feng Li, Jean-Jacques Gaumet, Pierre Magri, Sébastien Diliberto, Liang Zhou, and Liqiang Mai**

Supporting Information

Bottom-Up Confined Synthesis of Nanorod-in-Nanotube Structured Sb@N-C for Durable Lithium and Sodium Storage

Wen Luo, Feng Li, Jean-Jacques Gaumet, Pierre Magri, Sébastien Diliberto, Liang Zhou, Liqiang Mai**

Ms. W. Luo, Mr. F. Li, Prof. L. Zhou, Prof. L. Q. Mai
State Key Laboratory of Advanced Technology for Materials Synthesis and Processing, International School of Materials Science and Engineering, Wuhan University of Technology, Luoshi Road 122, Wuhan, 430070, P. R. China

Ms. W. Luo, Prof. J. J. Gaumet, Dr. P. Magri
Laboratoire de Chimie et Physique: Approche Multi-échelles des Milieux Complexes, Institut Jean Barriol, Université de Lorraine, Metz 57070, France

Dr. S. Diliberto
Institut Jean Lamour, UMR CNRS 7198, Université de Lorraine, Campus Artem, 2 allée André Guinier, Nancy 54000, France

Dr. L. Q. Mai
Department of Chemistry, University of California, Berkeley, California 94720, United States

E-mail : jean-jacques.gaumet@univ-lorraine.fr (Prof. J. J. Gaumet)
mlq518@whut.edu.cn (Prof. L. Q. Mai)

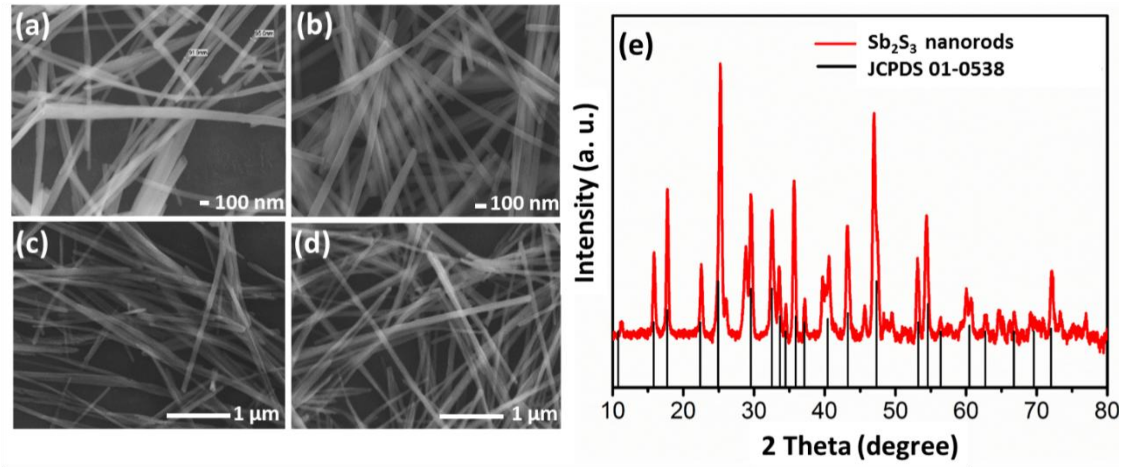

Figure S1. SEM images (a-d) and XRD pattern (e) of Sb_2S_3 nanorods.

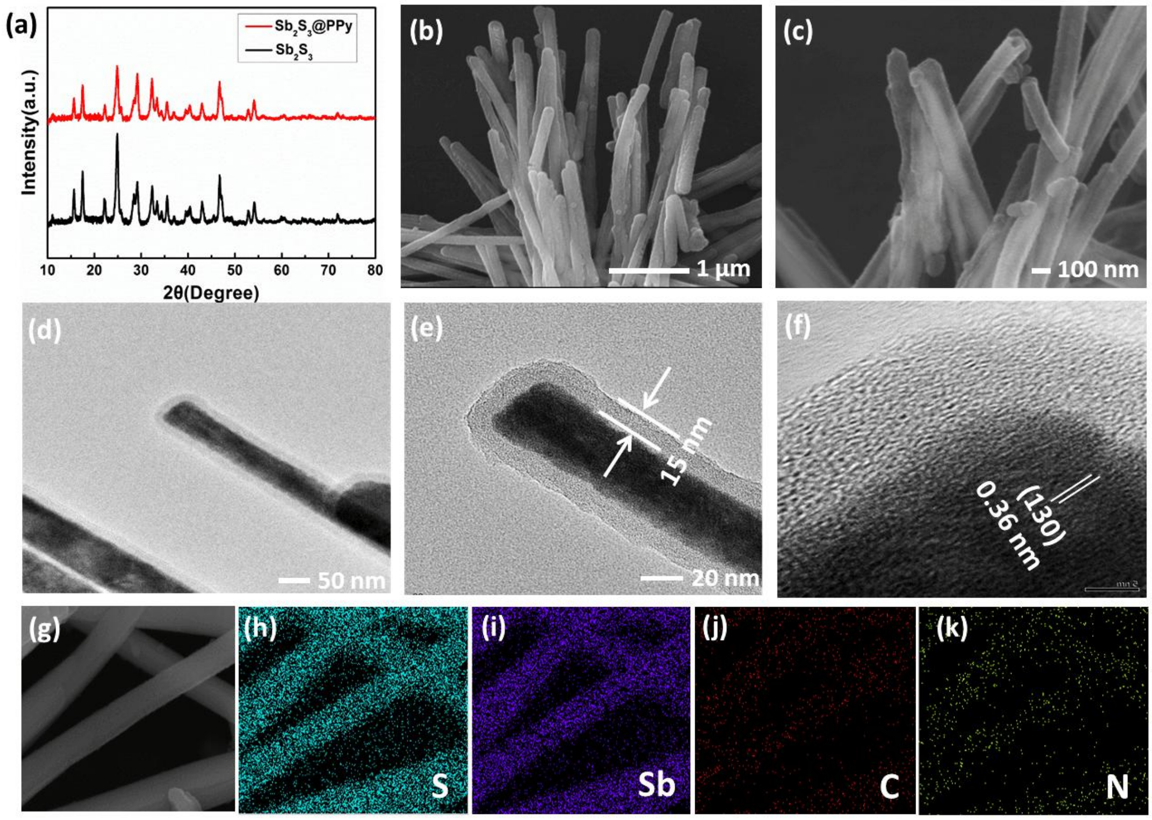

Figure S2. XRD pattern (a), SEM images (b, c), TEM images (d, e), HRTEM image (f) and corresponding elemental mapping images (g-k) of Sb_2S_3@PPy core-shell nanorods.

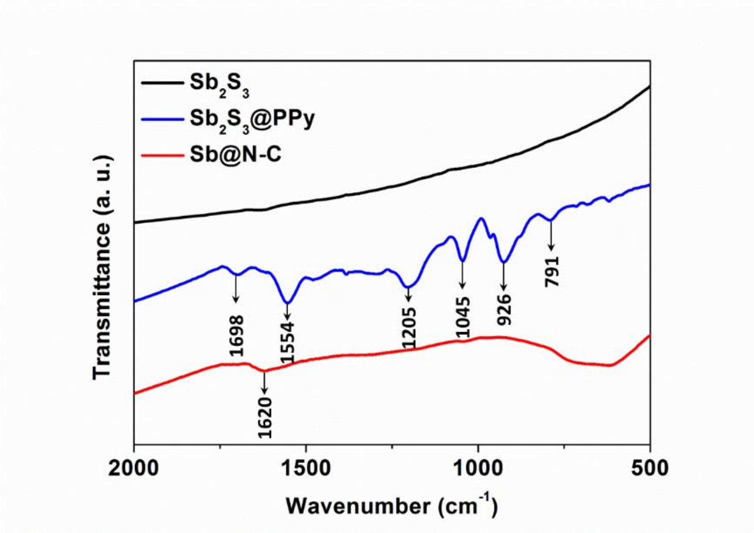

Figure S3. FTIR profiles of Sb_2S_3 nanorods, Sb_2S_3@PPy core-shell nanorods and Sb@N-C. The peak at 1698 cm^{-1} is ascribed to C–N bond and the peak at 1554 cm^{-1} is related to the C–C stretching. The breathing vibration of the pyrrole ring is confirmed by the peak located at 1205 cm^{-1}. The peak centered at 1045 and 926 cm^{-1} correspond to the in-plane and out-of-plane deformation vibrations of C–H band on the pyrrole ring, respectively. After calcination, the typical FTIR peaks of PPy polymer dismissed and a weak peak located at 1620 cm^{-1} can be attributed to C–N bond in the Sb@N-C composite.

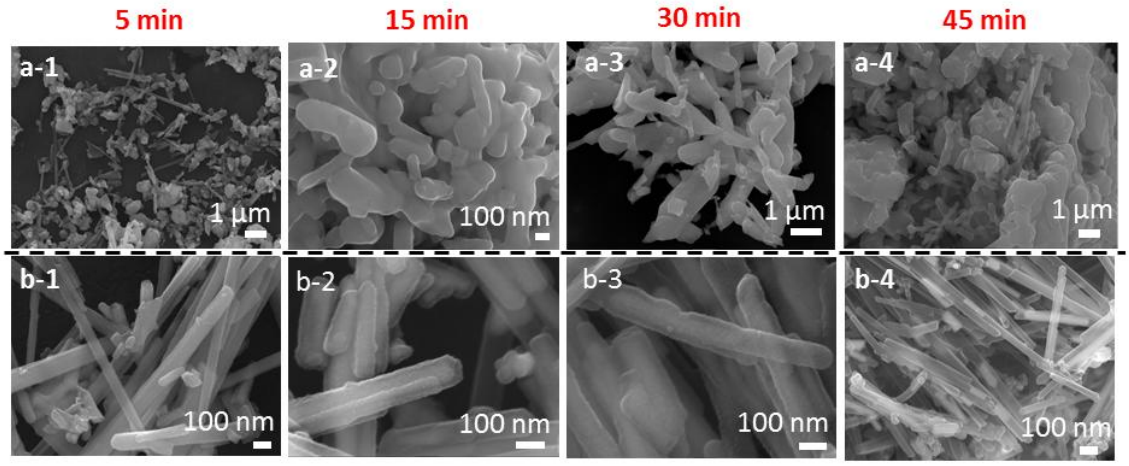

Figure S4. SEM images of bare Sb_2S_3 nanorods after annealing at 450 ^oC for 5 min (a-1), 15 min (a-2), 30 min (a-3) and 45 min (a-4). SEM images of Sb_2S_3@PPy nanorods after annealing at 450 ^oC for 5 min (b-1), 15 min (b-2), 30 min (b-3) and 45 min (b-4).

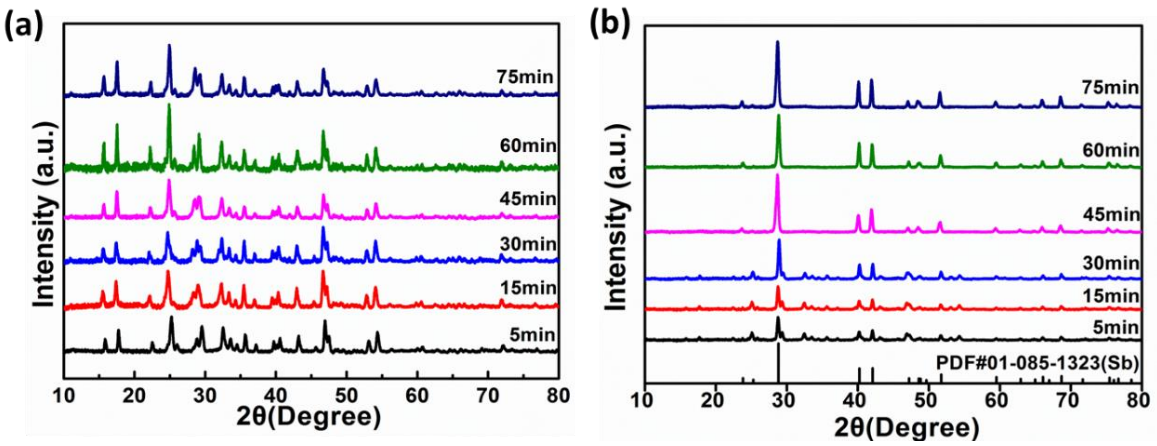

Figure S5. XRD patterns of Sb_2S_3 nanorods (a) and Sb_2S_3 @PPy core-shell nanorods (b) after annealing at 450 ^oC for 5, 15, 30, 45, 60 and 75 min.

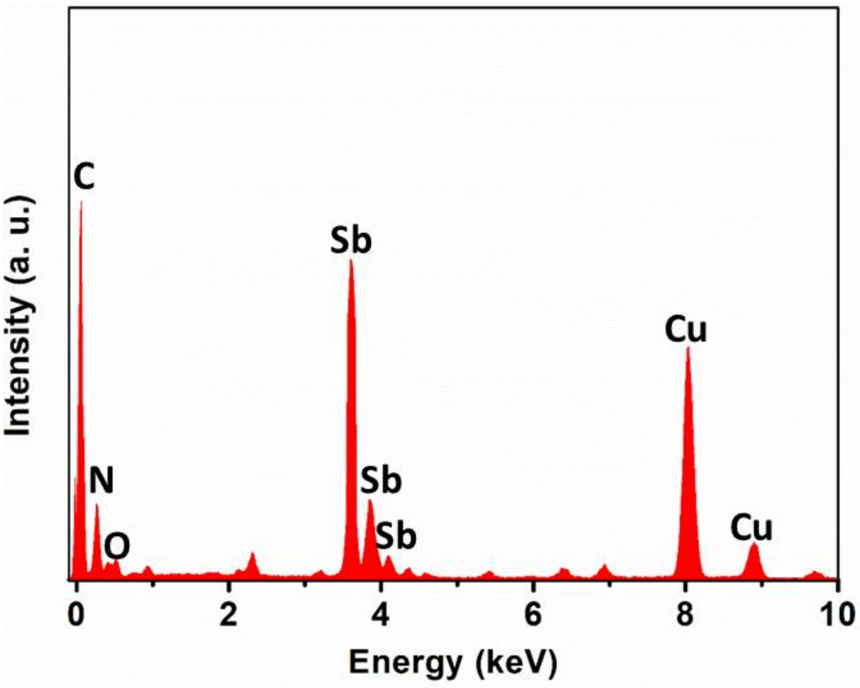

Figure S6. EDX spectrum of Sb@N-C.

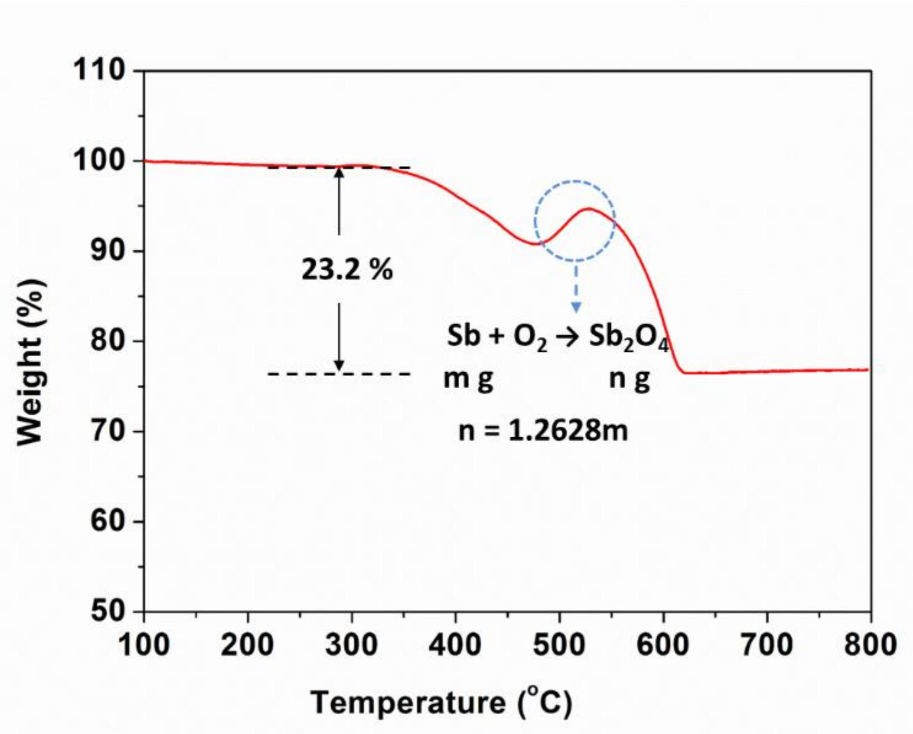

Figure S7. TGA curve of Sb@N-C hybrid in the air.

The Sb content was calculated based on the following equation:

$$\mathrm{Sb\ (wt\%)} = 100 * \frac{\text{molecular weight of Sb}}{\text{molecular weight of } \mathrm{Sb_2O_4}} * \frac{\text{final weight of } \mathrm{Sb_2O_4}}{\text{initial weight of Sb@N} - \text{CNT nanorods}}$$

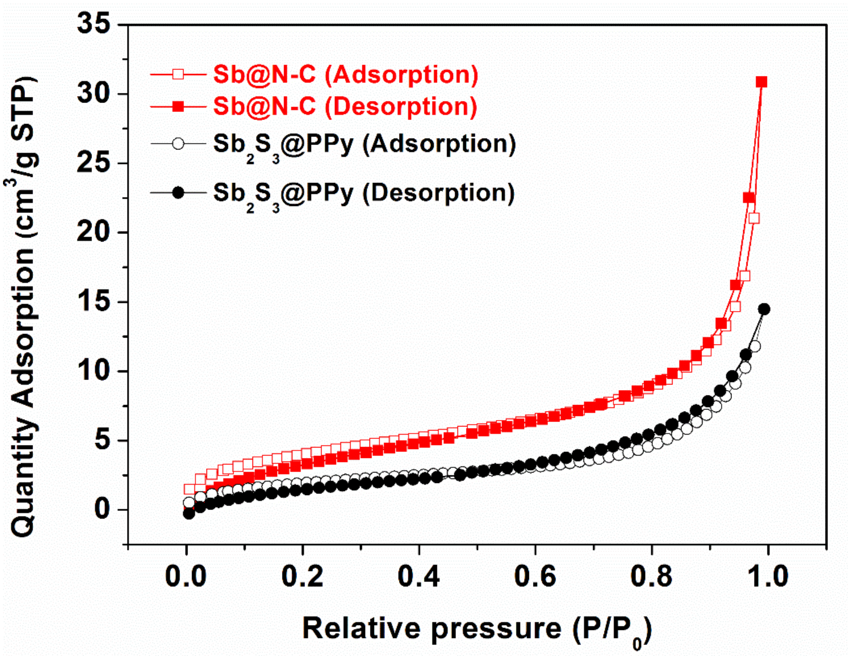

Figure S8. Nitrogen adsorption-desorption isotherms of Sb_2S_3@PPy and Sb@N-C.

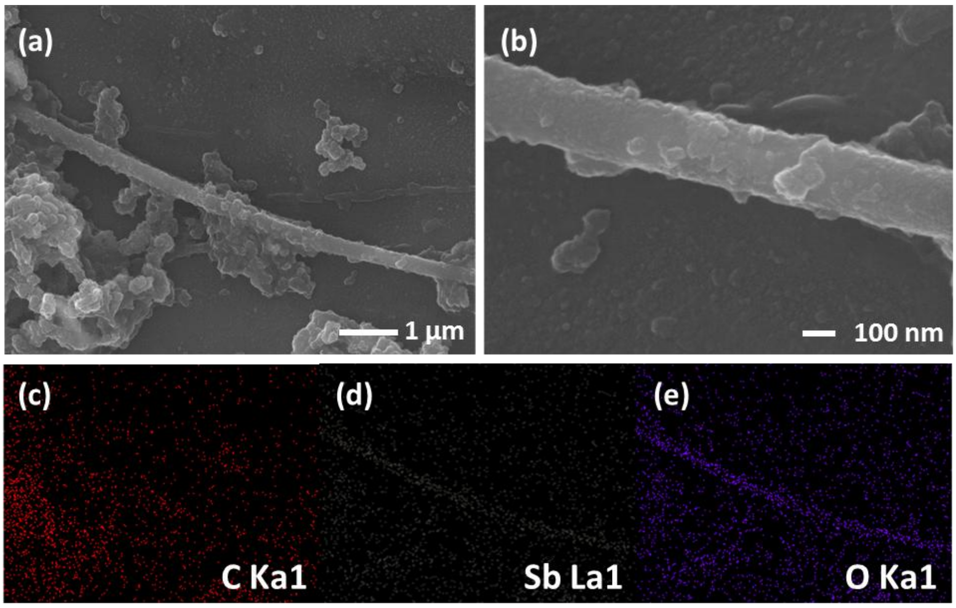

Figure S9. SEM images (a, b) and corresponding elemental mapping (c, d, e) of Sb@N-C hybrid after 300 cycles at a current density 200 mA g^{-1} in LIBs (delithiation state).

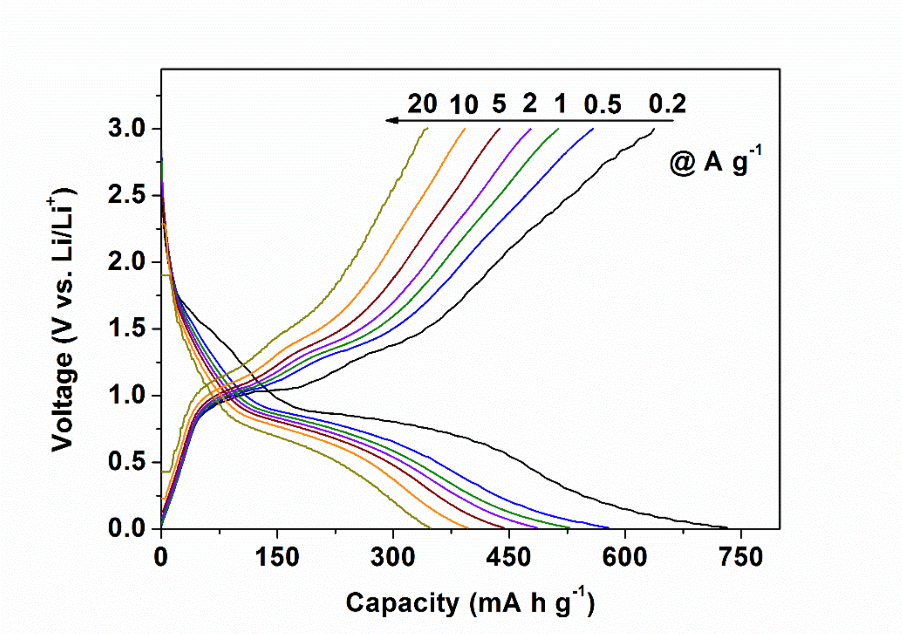

Figure S10. Typical lithiation-delithiation profiles when evaluating Sb@N-C anode in LIBs at various current densities.

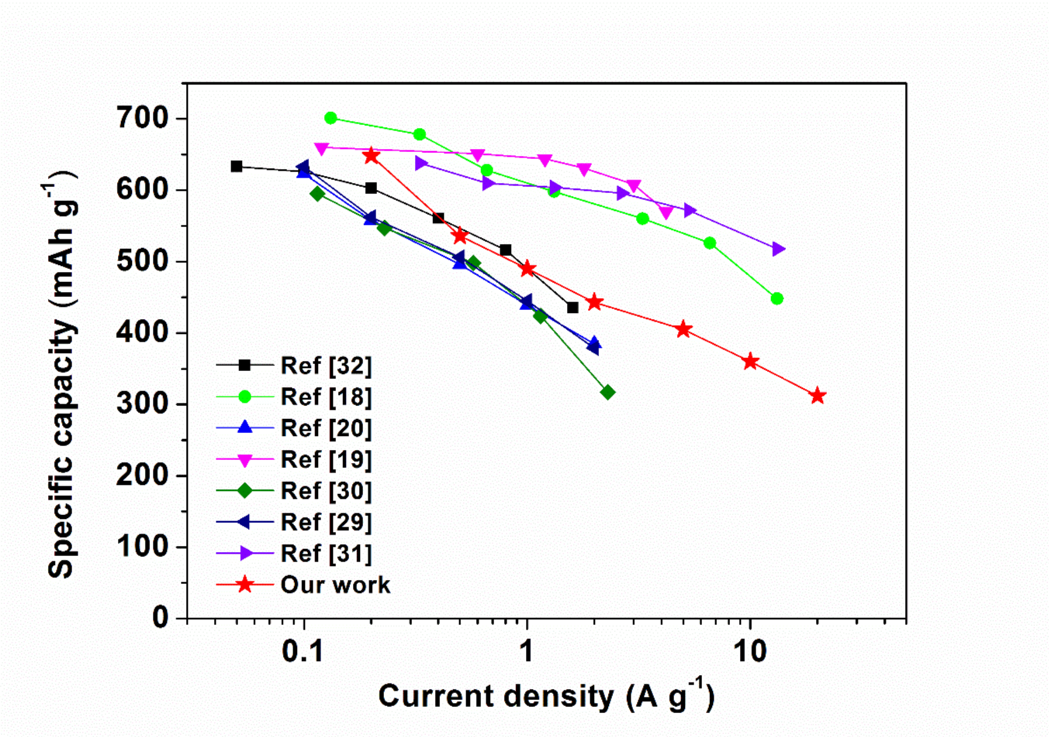

Figure S11. Comparison of the rate capability of Sb@N-C with previously reported Sb-based anodes for LIBs.

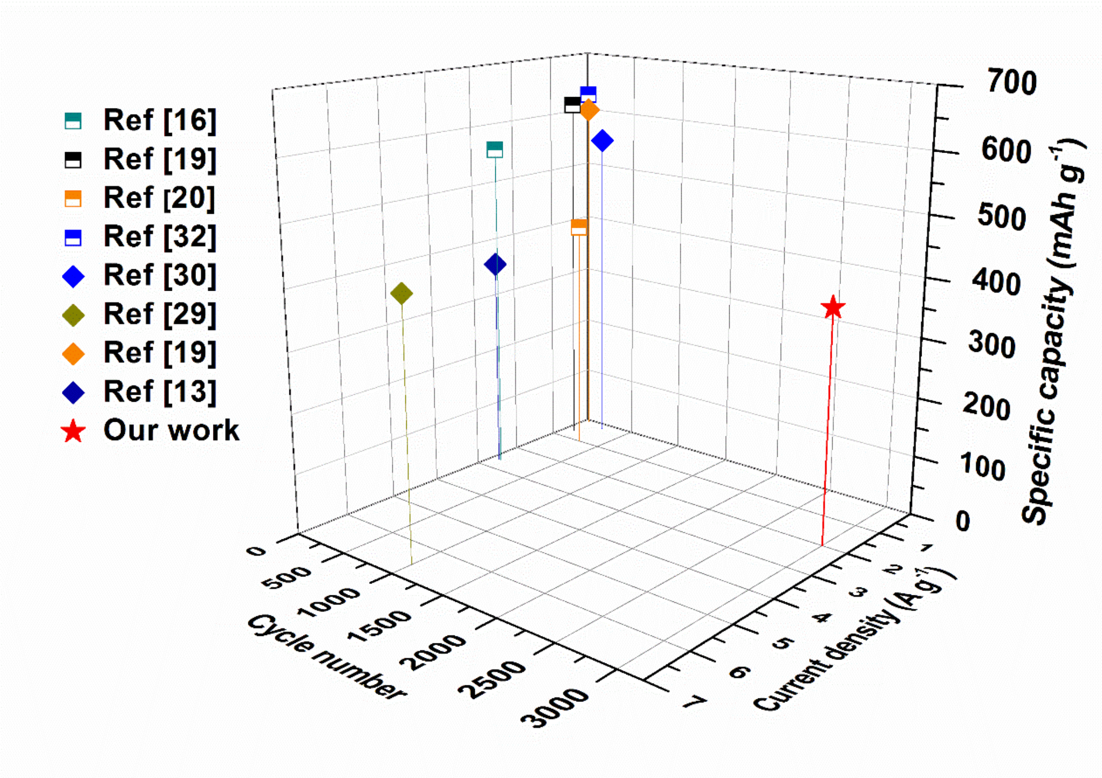

Figure S12. Comparison of the cycling performance of Sb@N-C with previously reported Sb-based anodes for LIBs.

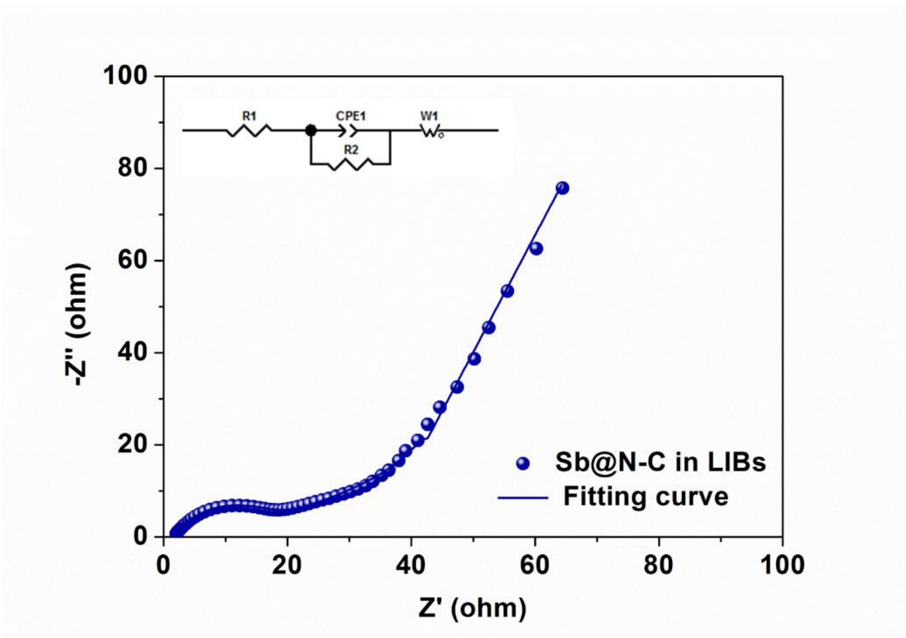

Figure S13. EIS plots and the fitting curve of Sb@N-C anode for LIBs

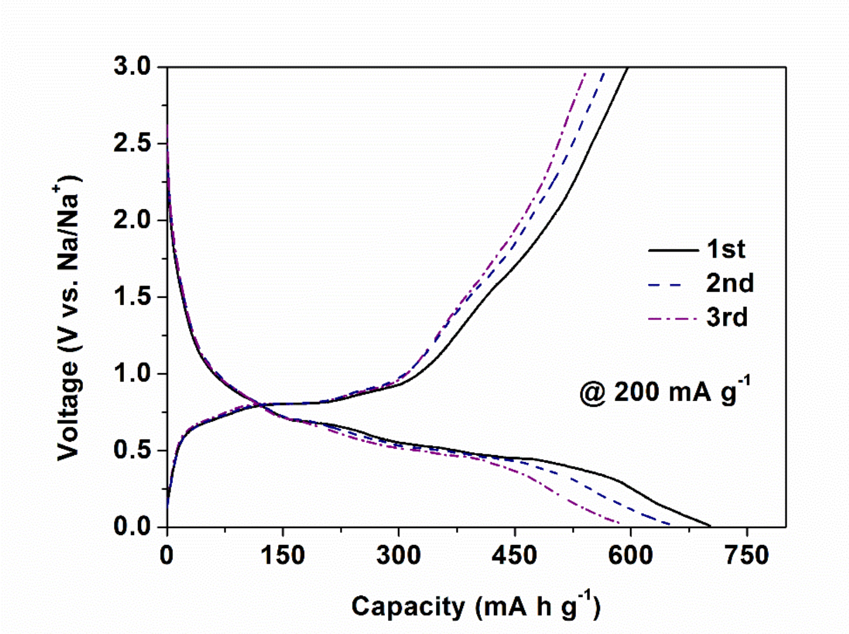

Figure S14. First three sodiation-desodiation voltage profiles of Sb@N-C anode for SIBs at a current density of 200 mA g^{-1}.

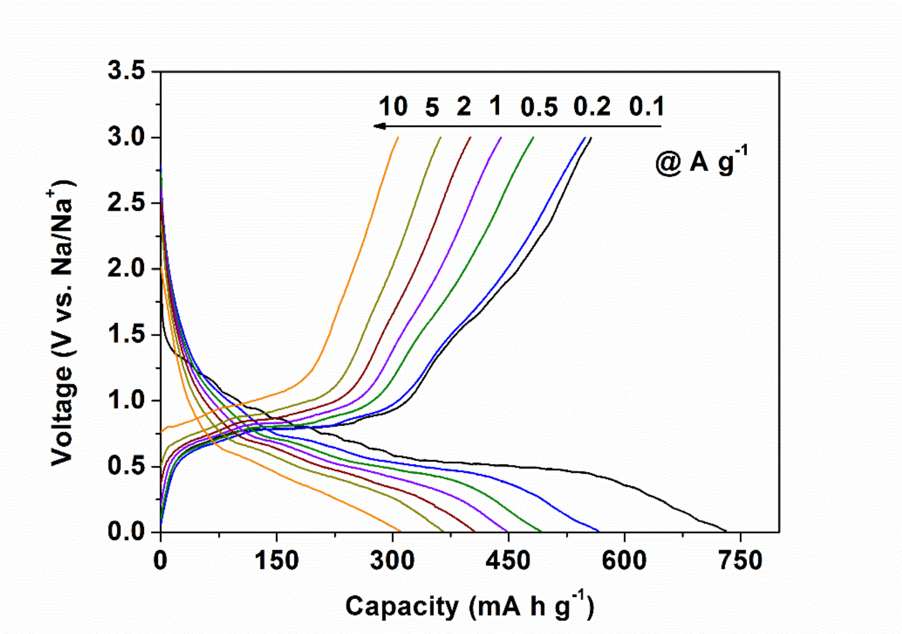

Figure S15. Typical sodiation-desodiation profiles when evaluating Sb@N-C anode in SIBs at various current densities.

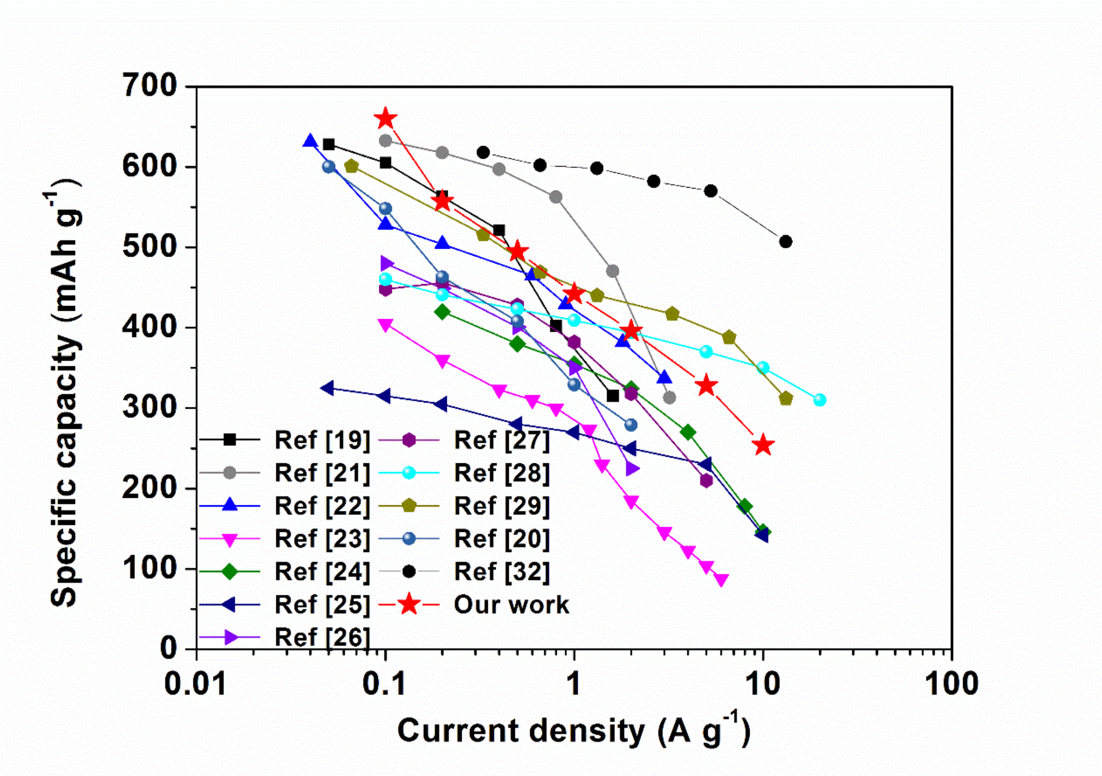

Figure S16. Comparison of the rate capability of Sb@N-C with previously reported Sb-based anodes for SIBs.

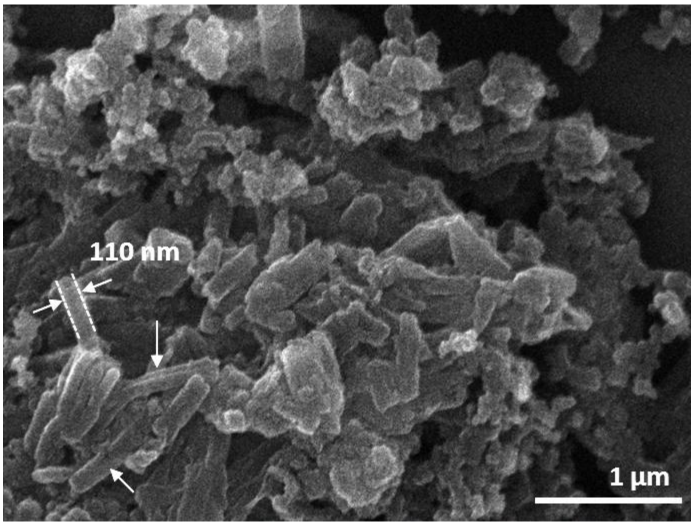

Figure S17. SEM images of Sb@N-C hybrid after long-term 3000 cycles at a current density of 2 A g^{-1} for SIBs (desodiated state).

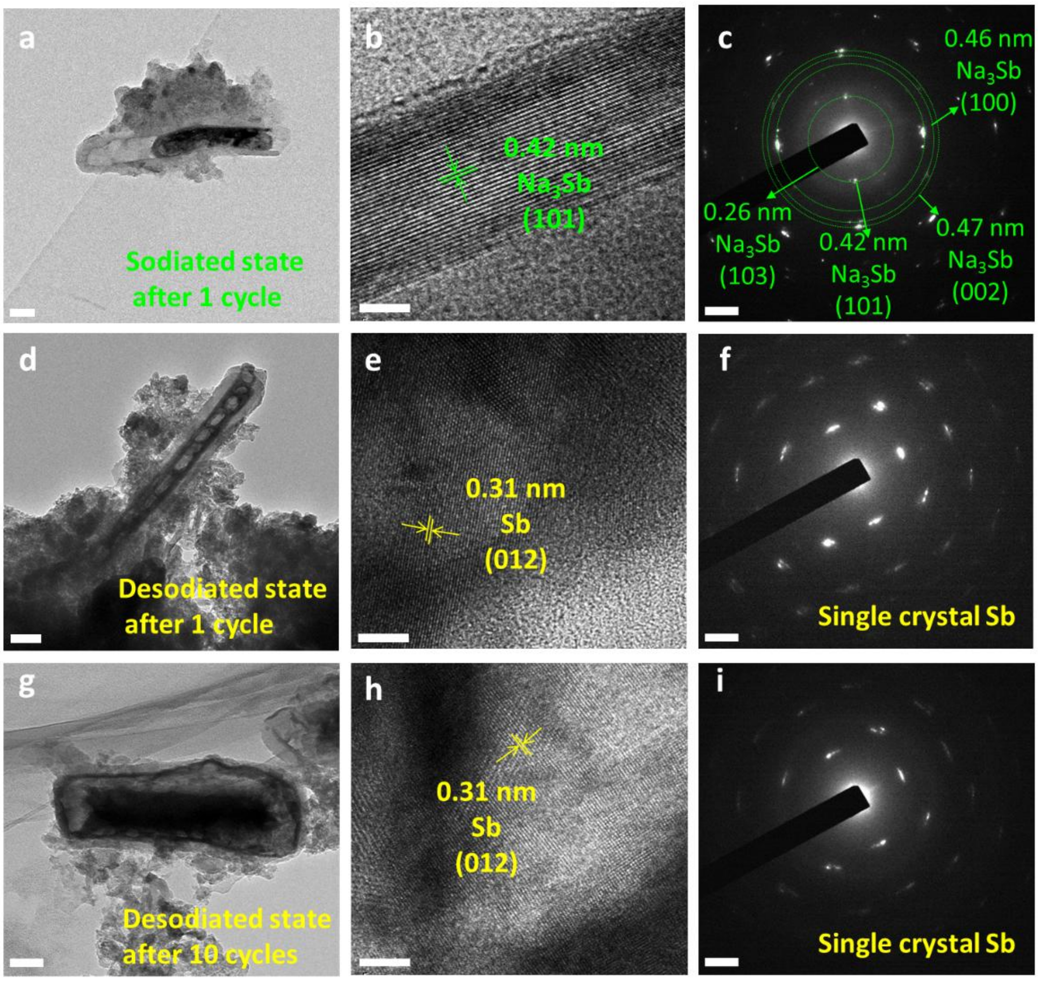

Figure S18. *Ex-situ* TEM measurement of Sb@N-C anode in SIBs: (**a-b**) TEM images and (**c**) SAED pattern of the Sb@N-C at sodiated state after 1 cycle at a current density of 200 mA g^{-1}; (**d-e**) TEM images and (**f**) SAED pattern of the Sb@N-C at desodiated state after 1 cycle at a current density of 200 mA g^{-1}; (**g-h**) TEM images and (**i**) SAED pattern of the Sb@N-C at desodiated state after 10 cycles at a current density of 200 mA g^{-1}. *Scale bars* **a, d, g** 100 nm; **b, e, h** 5 nm; **c, f, i** 2 nm^{-1}

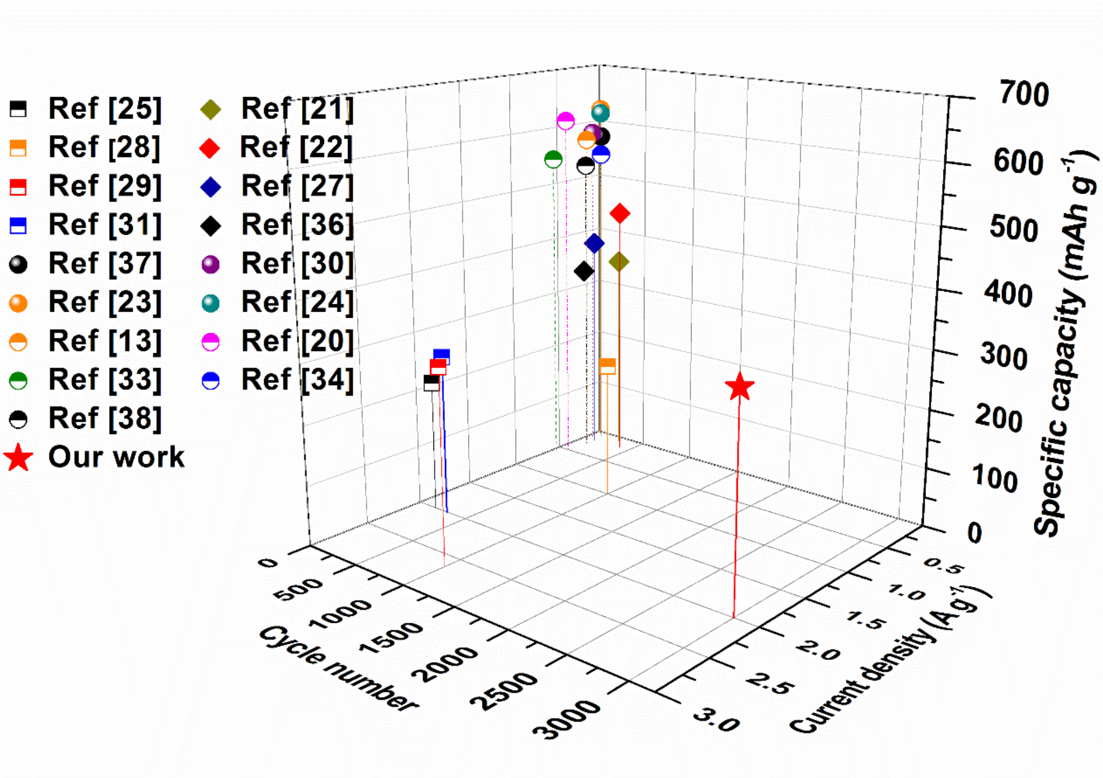

Figure S19. Comparison of the cycling performance of Sb@N-C with previously reported Sb-based anode for SIBs.

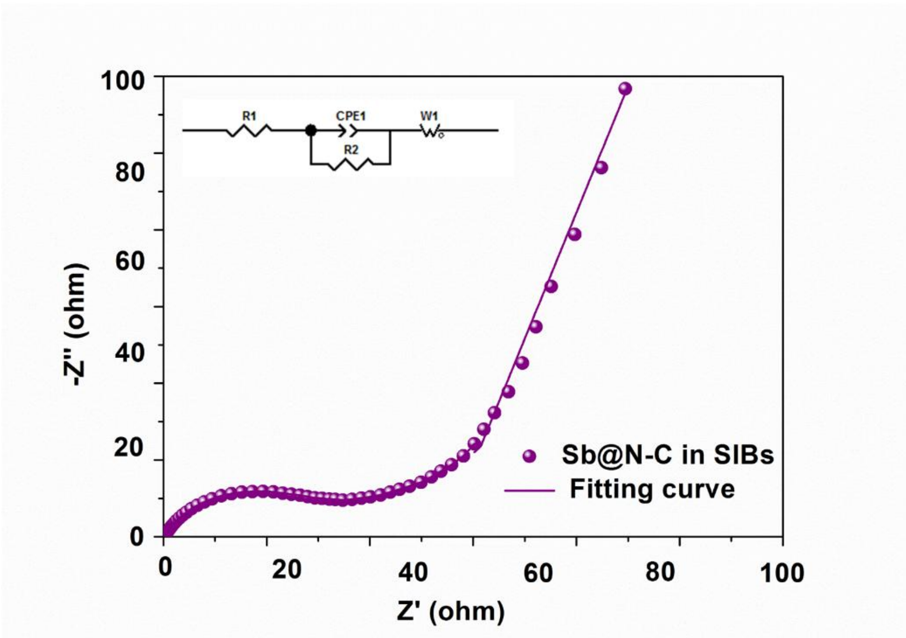

Figure S20. EIS plots and the fitting curve of Sb@N-C anode in SIBs.